Supporting Information

Briggs et al. 10.1073/pnas.0903535106

SI Text

SI Results. The lipid bilayer in HIV-1 particles appears different in areas where Gag is bound underneath, compared with areas where no Gag is bound (Fig. 1*A*), which has been suggested to represent a difference in the thickness of the lipid bilayer (1). To understand this effect, we generated a 40-Å-wide artificial bilayer profile, based on that described in ref. 2. To simulate the appearance of this bilayer in a tomographic reconstruction, we applied the contrast-transfer-function (CTF) of the microscope and filtered the data through the first node of the CTF. This calculation was performed for defocus values of −3.3 μm (similar to that used for the reconstruction here) (Fig. S1*A*) and of −6 μm (similar to that used in Fig. 1*A* and in ref. 1) (Fig. S1*B*). To simulate the matrix later we added a 30-Å-wide density to one side of the profile and repeated the calculation (dotted lines in Fig. S1). It can be seen that the presence of the extra protein layer leads to an apparent increase in the bilayer thickness at further-from-focus conditions. Closer to focus, the extra protein layer can be visualized as a thickening of the inner bilayer leaflet.

Supplementary Methods. ***cET.*** Samples were plunge-frozen on C-flat holey carbon grids by using an FEI vitrobot. Data were recorded by using an FEI Tecnai F30 "Polara" transmission EM, with Gatan GIF 2002 postcolumn energy filter and 2k×2k Multiscan CCD camera (Gatan). Data collection was performed at 300 kV with the energy filter in the zero-loss mode, and controlled by using the UCSF (University of California, San Francisco) tomography software. Tilt series were recorded from −63 ° to +63 ° with an increment of 3 °. The total dose was ≈70 $e^{-}Å^{-2}$. The defocus was between −2 and −5 μm. The nominal magnification was 27,500× or 34,000×, resulting in pixel sizes at the specimen level of 4.9 Å or 4.0 Å, respectively. Tomograms were reconstructed using the IMOD software (3).

Image analysis: Generation of initial model. These subtomograms were assigned an initial set of Euler angles based only on the geometry of the sphere (4), rotated according to these angles, and averaged. This average was used as a model for further alignment (in 6 dimensions, considering translation and rotation) and averaging steps during which the 6-fold symmetry present in the Gag lattice was applied. This procedure does not require the input of an arbitrary starting model.

For the in-vitro-assembled particles, this procedure was initially applied to 8 particles independently. Four of these particles converged to similar final structures which exhibited multiple nonapplied, 6-fold symmetry axes, as expected for a protein lattice. In each case, visualizing the final positions and orientations of the aligned subtomograms by using Amira (Visage Imaging), equipped with the EM package (5), showed that the structure was distributed over the surface of the particle to form a hexagonal lattice with appropriate angles. The presence of nonapplied symmetry axes in the final structure and the hexagonal distribution over the particle surface with appropriate angles provide verification of the structure because they would not be output by a model-biased, or otherwise misaligned, reconstruction. The 4 successful reconstructions were aligned to one another and averaged to generate an initial model. Immature virus was processed similarly: Three independent reconstructions of individual virus particles were aligned, averaged, and filtered to generate an initial model.

Image analysis: CTF correction. An initial estimate of the mean defocus of each tilt series was calculated from the average rotationally averaged power spectrum of all images. Due to variations of the defocus across the image and through the tilt series, a severe envelope function dampens the high frequencies, and only the position of the first node of the transfer function can be estimated. Each image in the tilt series was then corrected by defining the mean defocus of each image to be the mean defocus of the series and taking into account the defocus gradients across tilted images based on the tilt angle and orientation of the tilt axis. CTF-corrected tomograms were then generated by phase flipping using the initial estimate of the mean value, as well as ± 0.3 μm from the mean value. From each tomogram a reconstruction was calculated, and the resolution of the tomogram measured based on the Fourier shell correlation (FSC) curve. The mean defocus value giving the highest resolution reconstruction was selected.

Image analysis: Measurement of resolution. The dataset was split into 2 half-datasets and the FSC calculated. Three considerations avoid the possibility of an artificial resolution measurement. Firstly, any subtomograms that had shifted and rotated during their alignment to bring their overlapping regions together were removed because they could otherwise contribute identical data to the 2 halves of the dataset. Secondly, the flexibility of the lattice means that the resolution in the center of the reconstruction is higher than that at the edge of the reconstruction. A mask was therefore applied to the reconstruction, which had extremely soft edges to prevent a contribution of the mask itself to the correlation. Thirdly, frequencies correlated in the final reconstruction which were not considered during the alignment due to the application of the low-pass filter (Fig. 5*A*).

A comparison of the resolution of the reconstructions generated from CTF-corrected and -uncorrected data indicates an improvement from 21 Å to 17 Å after CTF correction.

Classification of regions of immature virus membrane with and without Gag bound. The final structure of one of the tomograms was edited to generate 2 models. In one model, the density of the Gag layer was increased by 20% relative to the density of the membrane, and in the other it was reduced by 20%. All data were then iteratively aligned and averaged against rotationally averaged forms of the 2 models by using a multireference alignment approach with each subtomogram reassigned after each iteration to one or other model based on maximum cross-correlation coefficient. This procedure was run until stable structures were generated. The positions of the 2 classes on the virus were visualized, and no correlation with the position of the missing wedge could be seen.

Lattice maps. Global lattice maps were visualized by placing a hexamer at the final-aligned coordinates using the EM package available for Amira (5). The list of subtomograms to be displayed was first edited to remove duplicate particles, as for the resolution measurement, and then to remove particles with radial positions substantially deviating from their neighbors. For figures, regions with no hexagonal order were removed by displaying only positions with 4–6 other hexamers within 15% of the mean lattice hexamer–hexamer spacing. Subtomograms with high cross-correlation were then displayed. This provided a robust separation of ordered and disordered regions.

Fitting and analysis. All fitting, structure analysis, and generation of Figs. 4–6 was carried out by using the UCSF Chimera package (6) from the Resource for Biocomputing, Visualization, and Informatics at the University of California, San Francisco (supported by National Institutes of Health Grant P41 RR-01081).

1. Wright ER, et al. (2007) Electron cryotomography of immature HIV-1 virions reveals the structure of the CA and SP1 Gag shells. *EMBO J* 26:2218–2226.
2. Wang L, Bose PS, Sigworth FJ (2006) Using cryo-EM to measure the dipole potential of a lipid membrane. *Proc Natl Acad Sci USA* 103:18528–18533.
3. Kremer JR, Mastronarde DN, McIntosh JR (1996) Computer visualization of three-dimensional image data using IMOD. *J Struct Biol* 116:71–76.
4. Forster F, Medalia O, Zauberman N, Baumeister W, Fass D (2005) Retrovirus envelope protein complex structure in situ studied by cryo-electron tomography. *Proc Natl Acad Sci USA* 102:4729–4734.
5. Pruggnaller S, Mayr M, Frangakis AS (2008) A visualization and segmentation toolbox for electron microscopy. *J Struct Biol* 164:161–165.
6. Pettersen EF et al. (2004) UCSF Chimera—A visualization system for exploratory research and analysis. *J Comp Chem* 25:1605–1612.

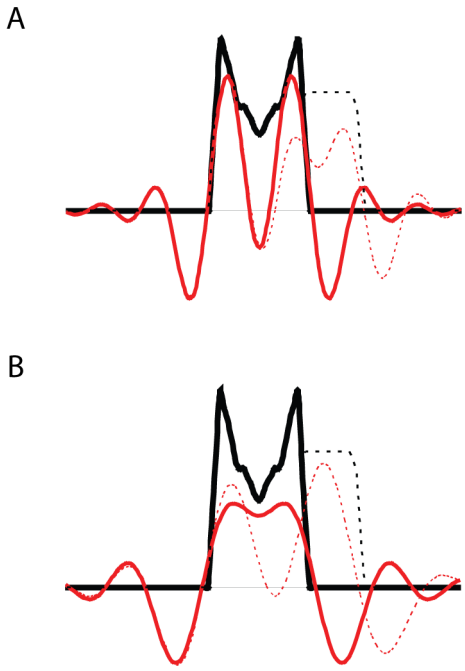

Fig. S1. Simulation of the effect of CTF and filtering on bilayer appearance. The density profile of a lipid bilayer with a protein bound (dotted lines) or without a protein bound (solid lines) is shown before (black lines) and after (red lines) application of the CTF of the microscope and a low-pass filter (see *SI Text* for further details). (*A*) Microscope defocus −3.3 μm. (*B*) Microscope defocus −6.0 μm.

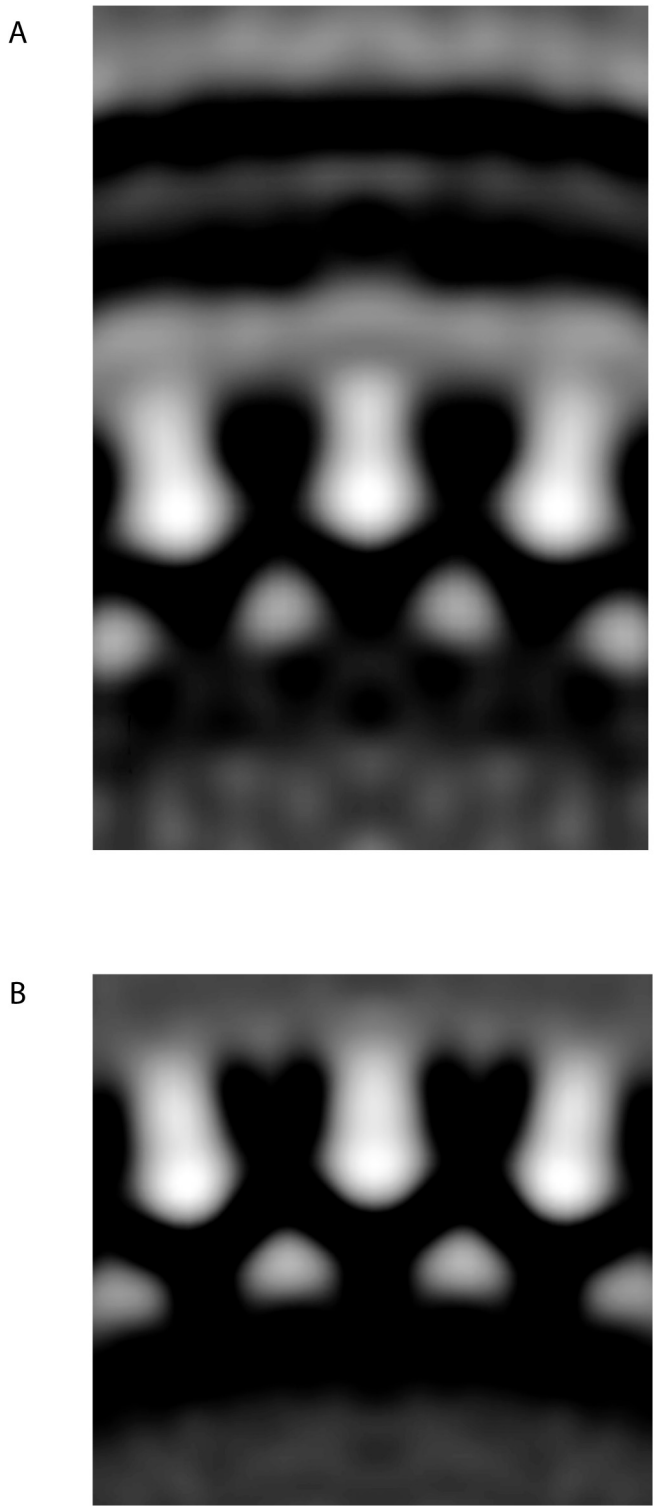

Fig. S2. Sections through the electron density of (*A*) the immature virus reconstruction and (*B*) the in-vitro-assembled particle reconstruction. These images correspond to Figs. 4*A* and 5*B*, respectively. Density is dark.

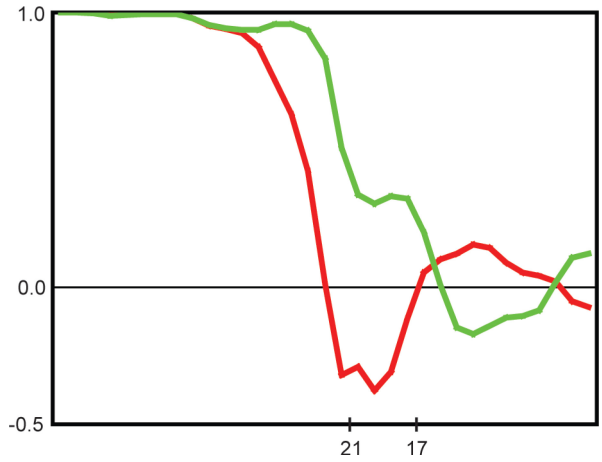

Fig. S3. Cross FSCs between 2 reconstructions at different defocuses, before (red) and after (green) correction of the CTF. Before CTF correction, regions of negative correlation are seen, which are absent after correction.

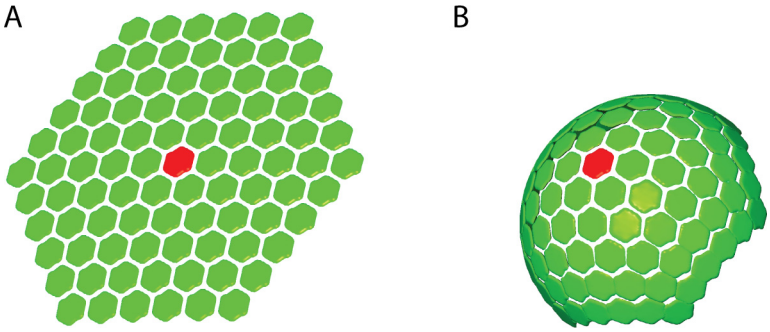

Fig. S4. A simple illustration of the effect of wrapping a hexameric lattice over a curved surface. (*A*) A flat lattice can grow indefinitely. (*B*) Curving the lattice leads to tighter packing of the hexamers further from the center.

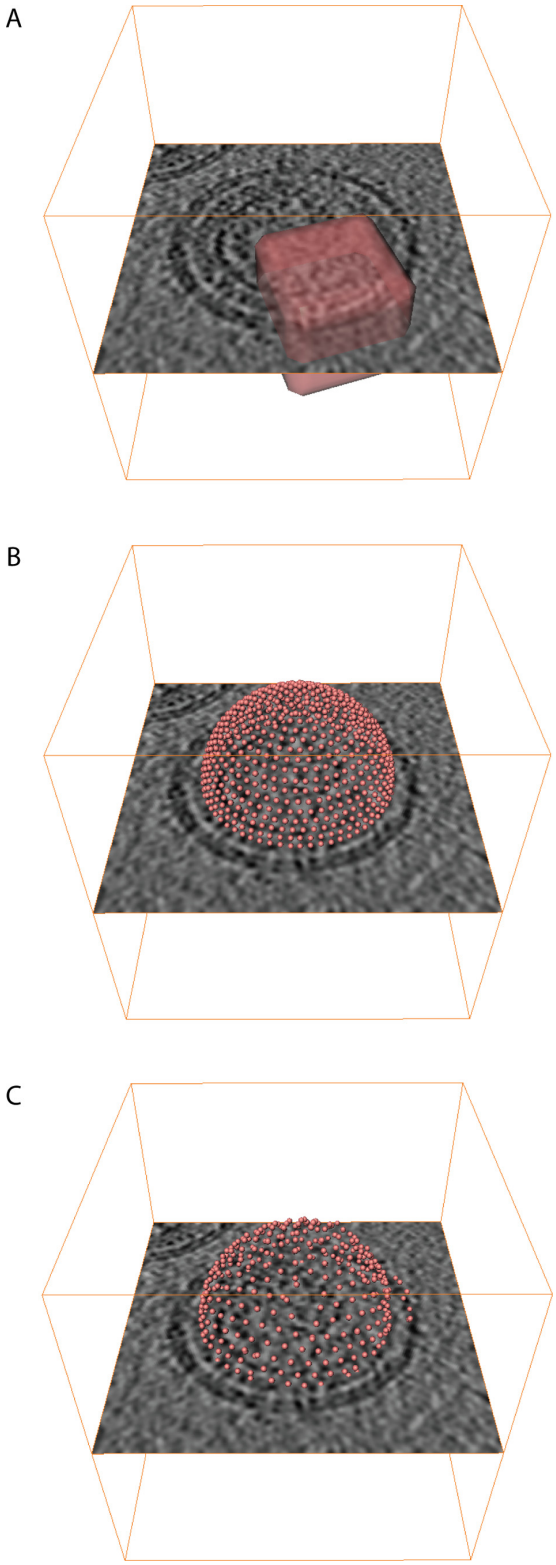

Fig. S5. Schematic overview of the subtomogram averaging method. (*A*) Subtomograms (transparent red box) are extracted from tomograms of virus particles (orange box with central section illustrated). (*B*) Tomograms are extracted with centers at the positions illustrated by the red points. (*C*) After alignment, the tomograms are centered at the red points shown here.